MOLECULAR IMAGING AND BIOLOGY

Mol Imaging Biol (2016) 18:70–78
DOI: 10.1007/s11307-015-0863-3

Published Online: 19 May 2015

RESEARCH ARTICLE

# *In Vivo* Detection of miRNA Expression in Tumors Using an Activatable Nanosensor

Byunghee Yoo,[1] Amol Kavishwar,[1] Alana Ross,[1] Pamela Pantazopoulos,[1] Anna Moore,[1,2] Zdravka Medarova[1,2]

[1]*Molecular Imaging Laboratory, MGH/MIT/HMS Athinoula A. Martinos Center for Biomedical Imaging, Massachusetts General Hospital and Harvard Medical School, Boston, MA, 02129, USA*
[2]*Department of Radiology, Massachusetts General Hospital and Harvard Medical School, Boston, MA, 02129, USA*

**Abstract**

*Purpose:* The development of tools for the analysis of microRNA (miRNA) function in tumors can advance our diagnostic and prognostic capabilities. Here, we describe the development of technology for the profiling of miRNA expression in the tumors of live animals.

*Procedures:* The approach is based on miRNA nanosensors consisting of sensor oligonucleotides conjugated to magnetic nanoparticles for systemic delivery. Feasibility was demonstrated for the detection of miR-10b, implicated in epithelial to mesenchymal transition and the development of metastasis. The miR-10b nanosensor was tested *in vivo* in two mouse models of cancer. In the first model, mice were implanted subcutaneously with MDA-MB-231-luc-D3H2LN tumors, in which miR-10b was inhibited. In the second model, mice were implanted bilaterally with metastatic MDA-MB-231 and nonmetastatic MCF-7 cells. The nanosensors were injected intravenously, and fluorescence intensity in the tumors was monitored over time.

*Results:* We showed that the described nanosensors are capable of discriminating between tumors based on their expression of miR-10b. Radiant efficiency was higher in the miR-10b-active tumors than in the miR-10b-inhibited tumors and in the MDA-MB-231 tumors relative to the MCF-7 tumors.

*Conclusions:* The described technology provides an important tool that could be used to answer questions about microRNA function in cancer.

**Key words:** Nanosensors, miRNA, Oligonucleotides, Activatable probes, Fluorescence, Magnetic nanoparticles, Cancer, Metastasis

## Introduction

As reported by Ling *et al.* [1], during the past decade, over 25,000 papers deposited on PubMed have reported on various aspects of microRNA (miRNA) genomics, biogenesis, mechanisms of action, pathway involvement, phenotypes in experimental models, and disease abnormalities. About 40 % of these publications have focused on the role of miRNAs in cancer. These studies have shown that miRNAs are dysregulated in almost all types of human cancer and specific signatures of aberrantly expressed miRNAs harbor diagnostic, prognostic, and therapeutic implications, including early diagnosis and staging, discrimination between different types of cancer, the identification of the tissue of origin of poorly differentiated tumors, prediction of chemotherapeutic response, *etc.*

Electronic supplementary material The online version of this article (doi:10.1007/s11307-015-0863-3) contains supplementary material, which is available to authorized users.

*Correspondence to:* Anna Moore; *e-mail:* amoore@helix.mgh.harvard.edu, Zdravka Medarova; *e-mail:* zmedarova@mgh.harvard.edu

These are all challenges that are still largely unresolved and the subject of intense clinical interest [1].

The overwhelming evidence in the literature of the value of miRNAs as cancer biomarkers underscores the importance of developing tools to understand how miRNAs participate in key aspects of carcinogenesis. Here, we describe technology that provides this capability in an *in vivo* setting. Specifically, we have developed nanosensors based on fluorescent turn-on oligonucleotide probes (oligos) sensitive to individual microRNA-mediated RNA interference [2]. The nanosensors consist of dextran-coated aminated iron oxide magnetic nanoparticles (MNs, 25–30 nm in diameter), conjugated to sensor oligos that are perfectly complementary to endogenous miRNA species. It is well known now that the choice between messenger RNA (mRNA) degradation and translational repression is dependent on the degree of complementarity between the mRNA target and the miRNA seed region [3]. Earlier, we had hypothesized and then confirmed [2] that sensor oligonucleotides perfectly complementary around the miRNA seed region would be cleaved in a sequence-specific way by the microRNA-RNA-induced silencing complex (RISC). In this work, we showed that a perfectly complementary sensor oligonucleotide specific to miR-10b is cleaved by miR-10b-RISC, despite the fact that all of miR-10b's known mRNA targets are bound with imperfect complementarity and regulated by translational repression and not mRNA cleavage. The sensor oligonucleotides are labeled with a fluorescent dye-quencher pair, so that upon cleavage of the oligonucleotide by the microRNA-RISC, fluorescence enhancement is observed.

We believe that the nanosensors have significant advantages over current technology. The currently established methods for microRNA detection *in situ* rely on PCR and northern blotting or high-affinity hybridization probes [4–14]. However, these methods are only applicable *in vitro*. Consequently, they do not permit longitudinal studies, in which the "evolution" of the tumor cell phenotype is monitored in an intact physiologic environment. In contrast, our approach offers the possibility for *in vivo* detection and monitoring. In addition, the existing methods rely on direct hybridization of the sensor oligo to the miRNA, reflecting a 1:1 ratio of fluorescent probe per miRNA. By contrast, our approach employs a powerful signal amplification strategy. Namely, consistent with our experience [15], each cell in this study is estimated to take up over $1\times10^6$ nanoparticles with attached sensor oligos. Each miRNA-RISC cleaves its complementary substrate oligo catalytically, leading to powerful signal amplification resulting from the cleavage of millions of synthetic substrates on the nanoparticles by the cognate miRNA-RISC complex [16, 17]. Finally, the described method, unlike approaches that rely on bioluminescent or fluorescent reporter gene expression [18–21], is composed of simple synthetic components that would one day make clinical applications more feasible. Also, unlike hybridization probes (*e.g.,* molecular beacons and SmartFlare, Millipore) the nanosensor does not remain stably bound to the miRNA and does not interfere with cellular function [2].

In the current study, we demonstrate the feasibility of the approach by focusing on miRNA-10b. miR-10b has been implicated in epithelial to mesenchymal transition and breast cancer metastasis by multiple studies including by our own group [22, 23–25]. Consequently, it is an attractive target with preclinical and clinical significance. Still, the technology can be utilized to measure the expression of any miRNA in any solid tumor model to answer questions related to cancer epigenetics. For example, it can be applied for monitoring the expression of microRNAs implicated in cancer progression and can be utilized in preclinical drug development. In particular, since microRNAs represent highly specific and/or early predictive biomarkers of metastatic potential, the technology could be used to gather information that could aid in forecasting invasive disease and predicting response to specific therapeutic modalities, leading to the design of individualized treatments. Clinically, the described technology could one day be used as a diagnostic and/or prognostic tool and support monitoring of treatment response [26–28].

## Materials and Methods

### *Sensor Oligonucleotide*

The sensor oligonucleotide (5′-5ThioMC6D/UUU/Cy5/CACAAA UUCGGUUCUACAGGGUA/IAbRQSp-3′) was designed to be perfectly complementary to the target miRNA, miRNA-10b, which plays a key role in epithelial-mesenchymal transition [23]. The backbone of the sensor oligonucleotide was composed of natural RNA bases. The 5′-end of the sequence was modified with Cy5 (fluorescent dye) and a spacer with three nucleic acids, which had a Thio-MC6-protected thiol group for the conjugation to MNs. Iowa Black RQ (quencher) was placed at the 3′-end of the sensor oligonucleotide. The oligo was synthesized by Integrated DNA Technologies (Coralville, IA).

### *Synthesis of Dextran-Coated MNs*

MN was synthesized following a protocol published previously [22]. Briefly, 30 ml of Dextan-T10 (0.3 g/ml, Pharmacosmos A/S, Holbaek, Denmark) was mixed with 1 ml of $FeCl_3{\cdot}6H_2O$ (0.65 g/ml, Sigma, Saint Louis, MO) while flushing argon gas for an hour. One milliliter of $FeCl_2{\cdot}4H_2O$ (0.4 g/ml, Sigma) was added to the mixture, and 15 ml of cold $NH_4OH$ (28 %, Sigma) was added dropwise to the stirred mixture. The temperature was increased to 85 °C for 1 h to start the formation of a nanoparticle dispersion and then cooled to room temperature. The magnetic nanoparticles were concentrated to 20 ml using Amicon ultra centrifugal units (MWCO 30 kDa; Millipore, Darmstadt, Germany). The resulting dextran-coated magnetic nanoparticles were cross-linked by epichlorohydrin (14 ml, 8 h, Sigma) and aminated with subsequent addition of

$NH_4OH$ (28 %, 60 ml). Aminated MNs were purified by dialysis and concentrated using Amicon ultra centrifugal units.

MN properties were as follows: Iron concentration was 10.94 mg/ml as determined using Total Iron Reagent Set (Pointe Scientific, Canton, MI); each nanoparticle contained 74 amine groups as determined by the *N*-succinimidyl 3-[2-pyridyldithio]-propionate (SPDP) quantification method; the size of MN was 20.3 ±0.6 nm as determined by dynamic light scattering (Zetasizer Nano ZS, Malvern Instruments Ltd., Westborough, MA).

## *Synthesis and Characterization of MN-miR-10b Nanosensor*

MN was sequentially conjugated to the heterobifunctional linker SPDP (Thermoscientific Co., Rockford, IL) and activated oligonucleotides. Briefly, 7.5 mg of SPDP was dissolved in 25 µl of anhydrous DMSO and incubated with MN, which has a maleimide group for thioether linkage with activated oligonucleotides. To release the thiol from the 5′-ThioMC6 linker and activate the oligonucleotides for conjugation, we used 3 % Tris(2-chloroethyl)phosphate (TCEP) treatment in nuclease-free phosphate-buffered saline (PBS). Activated oligonucleotides were purified using an ammonium acetate/ethanol precipitation method. After TCEP activation and purification, activated oligonucleotides were dissolved in nuclease-free water and incubated with the SPDP-modified MN overnight. The MN-miR-10b nanosensor was purified from unconjugated sensor oligonucleotide using a magnetic column (MACS 20 µ column, Miltenyi Biotech Inc., San Diego, CA).

The MN-miR-10b nanosensor was freshly prepared before each injection, and the number of oligonucleotides per MN was estimated as 3.0 by electrophoresis as described previously [22, 29]. The final size of the MN-miR-10b nanosensor was 22.2 ±0.3 nm.

## *Cells*

The human breast cancer cell line, MDA-MB-231-luc-D3H2LN, was purchased from Perkin Elmer (Hopkinton, MA) and cultured in Dulbecco's modified Eagle's medium (Sigma, Saint Louise, MO) supplemented with 10 % fetal bovine serum (FBS) (Thermo Scientific, Waltham, MA), 1 % antibiotics (Invitrogen, Carlsbad, CA), and 2 mM L-glutamine. The human breast cancer cell line MCF-7 was purchased from ATCC and cultured in RPMI 1640 medium with 5 % FBS and 1 % antibiotics, per the supplier's instructions (ATCC, Manassas, VA).

## *Fluorescence Activation by Nuclease A*

To test fluorescence activation of the synthesized nanosensor, we incubated it with specific nuclease.

Five microliters of purified nanosensor solution (10 µg Fe, 400 pmol as sensor oligo) was mixed with 92 µl of PBS buffer in a 96-well plate. The plate was read one time before the addition of 3 µl nuclease A (10 mg/ml, 700 U/ml, Qiagen, Hilden, Germany). The reading was repeated according to a prefixed schedule to obtain the maximum fluorescence activation after the addition of nuclease A. The fluorescence spectra were collected using the following parameters: excitation wavelength—600 nm, emission wavelength—640–800, cutoff—630 nm, interval—2 nm, acquisition number—6.

## *Animal Model*

The miR-10b-inhibited tumor model was generated as described in [22]. Briefly, six-week-old female old nude mice ($n$=5) were implanted subcutaneously with MDA-MB-231-luc-D3H2LN cells ($2\times10^6$ cells in the right flank). When tumors reached a diameter of ~0.5 cm, the animals were injected intravenously with a miR-10b inhibitor (MN-anti-miR-10b, nanoparticles carrying locked nucleic acid binding to miR10-b) or an inactive control (MN-scr-miR, nanoparticles carrying irrelevant locked nucleic acid) to generate the miR-10b inhibited group or active group, respectively. This treatment leads to complete inhibition of miR10-b as we have shown in our previous work [22].

For the bilateral tumor model, six-week-old female athymic nude mice ($n$=5) were treated with estradiol cypionate (3 mg/kg) in cottonseed oil for 2 weeks and implanted subcutaneously in the flanks with MDA-MB-231-luc-D3H2LN ($2\times10^6$ cells) and MCF-7 ($2\times10^6$ cells). All animal experiments were performed in compliance with institutional guidelines and approved by the Institutional Animal Care and Use Committee (IACUC) at Massachusetts General Hospital.

## *Fluorescence/Bioluminescence Optical Imaging*

Imaging was performed using the IVIS Spectrum imaging system (Perkin Elmer, Hopkinton, MA). Anesthetized mice were intravenously injected with MN-miR-10b nanosensor (15 mg/kg Fe; 1.7 mg/kg sensor oilgo) and scanned 1, 3, 5, 7, 9, 11, 13, 18, 24, and 40 h after injection. The acquisition conditions for fluorescence imaging were as follows: exposure time—0.5 s; binning factor—8; excitation filter range—570, 605, 640, and 675 nm; emission filter range—640, 660, 680, 700, and 720 nm; $f$ number—2. Spectral unmixing (Living Image ver. 4.4) was employed to minimize the influence of tissue autofluorescence. Radiant efficiency was measured for the same region of interest (ROI) in all images. At the end of the fluorescence imaging session, mice were injected intraperitoneally with D-luciferin potassium salt in DPBS (200 µl of 15 mg/ml; Perkin Elmer, Hopkinton, MA). Identical imaging acquisition settings (time, 0.5~60 s; F-stop—2; binning—medium) and the same regions of interest (ROIs) were used to obtain total radiance (photons/s/$cm^2$/sr) from the tumors.

## *Real-Time Quantitative Reverse Transcription-PCR*

Surgically removed primary tumor tissues were homogenized to extract the miRNA-enriched fraction. Relative levels of miR-10b were determined by real-time quantitative reverse transcription-PCR (qRT-PCR; Taqman protocol) and compared to the internal housekeeping gene, SNORD44. Taqman analysis was carried out using an ABI Prism 7700 sequence detection system (Applied Biosystems, Foster City, CA). The primers (Hs-miR-10b-3 miScript Primer, Hs-SNORD44-11 miScript Primer) and assay kit

(miScript PCR Starter Kit) were purchased from Qiagen. Relative expression was calculated by the ΔΔCt method.

### *Fluorescence Microscopy of Tissue Sections*

Excised tumor tissues were embedded in Tissue-Tek OCT compound (Sakura Finetek, Torrance, CA) and snap frozen in liquid nitrogen. The tissues were cut into 7-μm sections. The slides were counterstained and mounted with Vectashield mounting medium with (4′,6-diamidino-2-phenylindole (DAPI) (Vector Laboratories, Inc. Burlingame, CA). To determine MN-miR-10b accumulation in tissue, the sections were analyzed by fluorescence microscopy using a Nikon Eclipse 50i fluorescence microscope (Nikon, Tokyo, Japan), equipped with the necessary filter sets (Chroma Technology Corporation, Bellows Falls, VT). Images were acquired using a charge-coupled device camera with near-IR sensitivity (SPOT 7.4 Slider RTKE; Diagnostic Instruments, Sterling Heights, MI). The images were analyzed using SPOT 4.0 Advance version software (Diagnostic Instruments, Sterling Heights, MI).

### *Statistical Analysis*

Data were expressed as mean±SD. Statistical comparisons were drawn using a two-tailed *t* test (SigmaStat 3.0; Systat Software, Richmond, CA). A value of $p<0.05$ was considered statistically significant.

## Results

### *General Design and Mechanism*

The design of the MN-miRNA nanosensor is based on our prior publications [30, 31] [22] in which we have described the development and application of oligonucleotide-modified nanoparticles for the targeting of the RNAi mechanism in tumor cells. Specifically, the nanosensor consists of MNs (~20 nm in diameter), conjugated to sensor oligos [2] that are perfectly complementary to endogenous miRNA species (Fig. 1a). The design and testing of the prototype sensor oligos have recently been described by us [2]. Specifically, the sensor oligonucleotides are composed of RNA bases and are cleavable (nonstabilized by chemical modification) around the seed region (the conserved region within which the microRNA engages the RNA substrate). The oligonucleotide strand is labeled with a fluorescent dye-quencher pair, so that upon its cleavage by the microRNA-RISC, the dye-quencher pair separates resulting in dequenching and fluorescence enhancement (Fig. 1a). In our prior study, we demonstrated the feasibility of accurately detecting miRNA expression in a cell-free system and intact cells *in vitro* using the described sensor oligonucleotide design and extensively validated our hypothesis that fluorescence enhancement resulted from specific cleavage of the sensor oligo by the miR-primed RISC [2].

For *in vivo* delivery, the oligo was conjugated to the nanoparticles. Nanosensor accumulation in the tumor is driven by the innate pathways of hemodynamics and biodistribution characteristic for the nanoparticles and governed by the well-established enhanced permeability and retention (EPR) effect, as indicated by our earlier work [29, 30]. The specific mechanism of nanosensor action is described in Fig. 1b. Namely, following intravenous injection, the long-circulating nanoparticles distribute through the circulation and progressively accumulate in the tumor interstitium due to its hyperpermeable vasculature and compromised lymphatic drainage (EPR effect) [32]. Once inside the tumor interstitium, the nanoparticles are endocytosed by the tumor cells through macropinocytosis

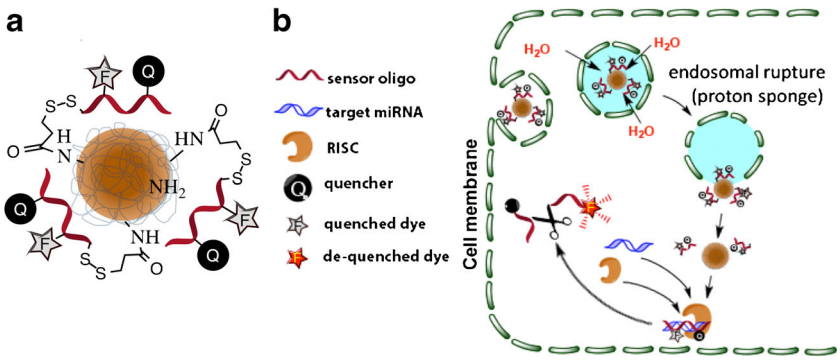


**Fig. 1** Nanosensor design and mechanism of action. **a** The nanosensor consists of magnetic nanoparticles (MNs), conjugated to sensor oligos that are perfectly complementary to endogenous miRNA species. These sensor oligonucleotides are composed of RNA bases and are cleavable (nonstabilized by chemical modification) around the seed region (the conserved region within which the microRNA engages the RNA substrate). The oligonucleotide strand is labeled with a fluorescent dye-quencher pair, so that upon its cleavage by the microRNA-RISC, the dye-quencher pair separates producing dequenched fluorescence enhancement. **b** In the cytosol, the nanoparticles, which carry a sensor oligo complementary to an endogenous microRNA species, bind the microRNA, leading to the recruitment to the endogenous RNA-induced silencing complex (RISC) and cleavage of the oligo at a specific position in the seed region. This cleavage results in separation between the quencher and dye located at the ends of the sensor oligo and fluorescent turn-on. The microRNA is released from the complex and is free to catalyze subsequent cleavage reactions.

and localize to endosomes [29]. Inside endosomes, the functionalized nanoparticles rich in unsaturated amines mediate the proton sponge effect leading to endosomal rupture and nanosensor deposition in the cytosol [33]. In the cytosol, the nanoparticles, which carry a sensor oligo complementary to an endogenous microRNA species, bind the microRNA based on complementarity to its seed region, leading to the recruitment to the endogenous RISC and cleavage and degradation of the oligo. This cleavage results in separation between the quencher and dye located at the ends of the sensor oligo and fluorescent turn-on. The microRNA is released from the complex and is free to catalyze subsequent cleavage reactions [2].

The described mechanism exploits the endogenous process of RNA interference and takes advantage of powerful signal amplification. Namely, a single miRNA will cleave numerous substrate oligos, since RNAi is a "catalytic" molecular mechanism. In addition, a single nanoparticle can carry up to 40 substrate oligos, taking advantage of the phenomenon of multivalency [34, 35]. Finally, the number of nanoparticles taken up by the tumor cells is large ($15\times10^6$ nanoparticles/cell) [15].

## *The MN-miRNA Nanosensor Is Functional*

To assess the feasibility of the approach, we designed a nanosensor that can detect the expression of miRNA-10b. miR-10b has been implicated in epithelial to mesenchymal transition and breast cancer metastasis by multiple studies including by our own group [22, 23–25]. Consequently, the capacity to detect miR-10b expression in tumor cells can have an important preclinical and clinical impact.

To demonstrate that the nanosensor was synthesized as designed and to prove successful incorporation of the sensor oligonucleotide into the nanosensor, after purification, the nanosensor was treated with a reducing agent (TCEP). Electrophoretic analysis confirmed the successful release of the disulphide-conjugated sensor oligonucleotide from MN following TCEP treatment. No free sensor oligonucleotide was detected in the absence of TCEP, indicating that in the final nanosensor preparation, the sensor oligonucleotides were conjugated to MN (Fig. 2a).

Having previously established that the sensor oligo can report on miRNA expression in tumor cells [2], we next set out to determine if conjugation to the nanoparticle carrier preserves the functionality of the oligo. Figure 2 illustrates the activation of the MN-miR-10b nanosensor by nuclease treatment *in vitro*. The nanosensor was incubated with excess RNAse A to simulate the catalytic activation of sensor oligonucleotide. As a control, the MN-miR-10b nanosensor was incubated in nuclease-free water. These results showed an over fourfold increase in fluorescence after incubation with RNAse A, indicating that conjugation to the MN carrier does not interfere with sensor oligo activation (Fig. 2b).

## *The MN-miRNA Nanosensor Can Report on miRNA Expression In Vivo*

To determine the feasibility of detecting miRNA expression *in vivo*, we first generated an animal model in which miR-10b expression in the tumors was either left active or inhibited, as described in [22]. We injected the nanosensor intravenously into tumor-bearing animals and performed whole-body fluorescence reflectance imaging over a time course of 0 to 24 h using filters for the Cy5 dye on the sensor oligo. Bioluminescence imaging (BLI) for the accurate delineation of viable tumor mass was also performed.

We observed clear enhancement of the primary tumor, consistent with cleavage of the sensor oligo, separation of the Cy5 dye from the quencher, and a fluorescent turn-on (Fig. 3a). This effect was specific for miR-10b, since in the animals in which miR-10b was inhibited, the signal enhancement was significantly lower than in the animals in which miR-10b was active.

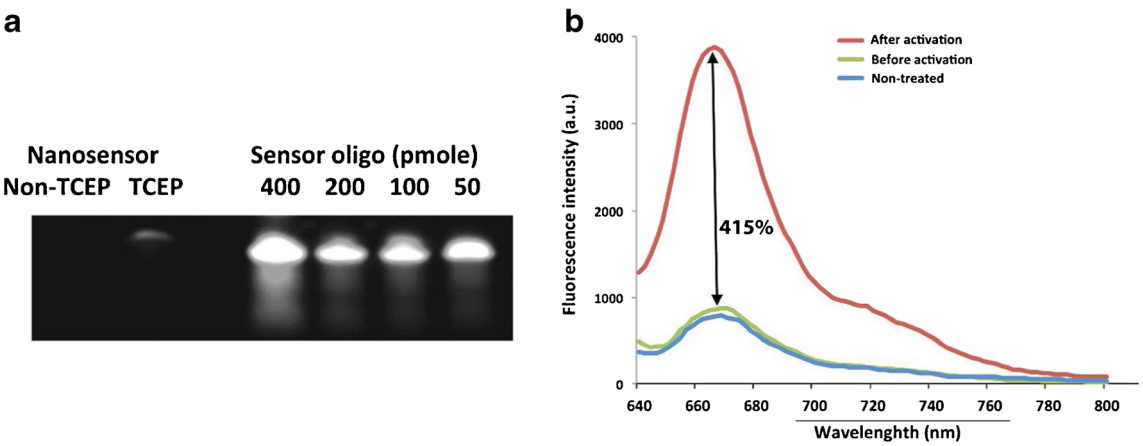


**Fig. 2** Activation of fluorescence and the release of the sensor oligonucleotide from the MN-miR-10b nanosensor. **a** Electrophoresis confirmed the release of sensor oligonucleotides from MN after TCEP treatment. **b** Cleavage of the sensor oligo on the nanosensor by nuclease A leads to a 415 % increase in fluorescence intensity over the background.

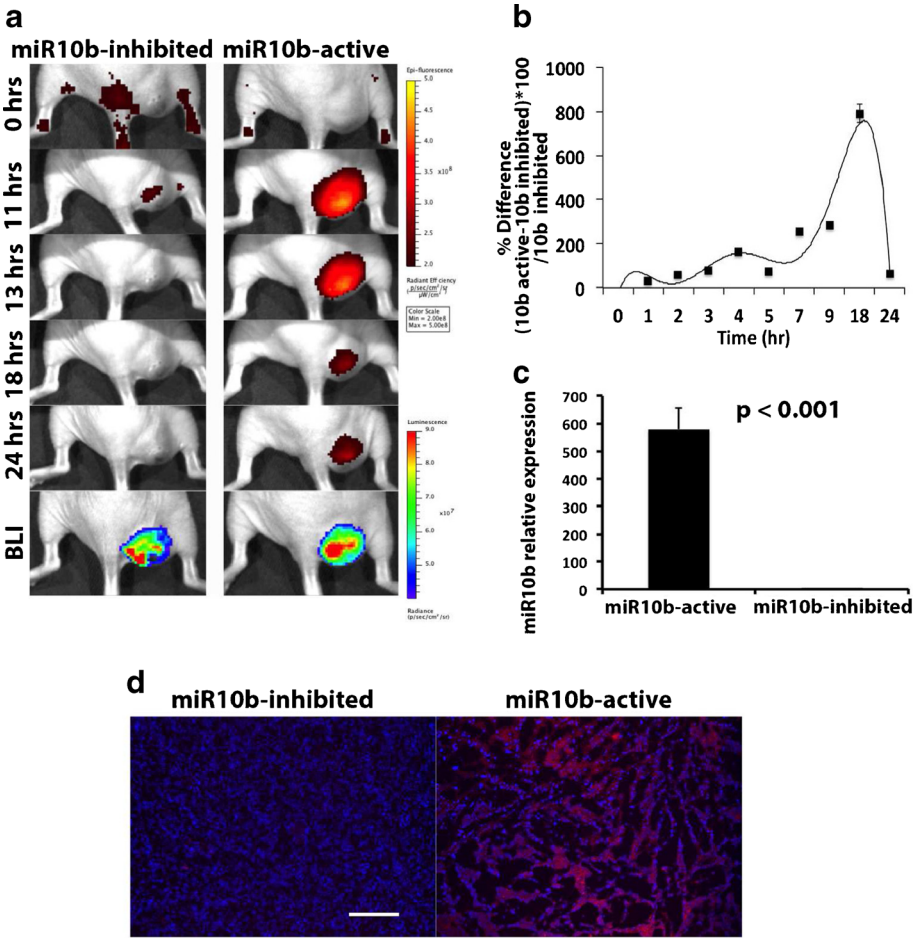


**Fig. 3** *In vivo* detection of miR-10b expression in a miR-10b-inhibited breast tumor model. **a** Fluorescence optical imaging showing significantly higher fluorescence intensity in the tumors in which miR-10b was left active over the miR-10b-inhibited tumors (i.v., 15 mg/kg Fe; 1.7 mg/kg sensor oilgo). Tumor ROIs are color-coded according to radiant efficiency. **b** Quantification of radiant efficiency from A indicated a peak of fluorescence activation in the miR-10b-active tumors at 18 h after nanosensor injection. **c** qRT-PCR of miR-10b expression in the miR-10b-active vs miR-10b-inhibited tumors demonstrated a significant difference between the two groups (data represent average±SD; two-tailed *t* test; $n$=3). **d** Fluorescence microscopy of tumor tissue from mice injected with the nanosensor. Cy5 fluorescence from the activated nanosensor was seen in the miR-10b-active tumors but not the miR-10b-inhibited tumors (blue—DAPI, nuclei; red—Cy5, activated nanosensor).

Quantitative assessment of relative radiance efficiency revealed that the maximal difference between miR-10b-inhibited and miR-10b-active tumors was achieved 18 h after nanosensor injection (Fig. 3b, 790±70 % enhancement at the 18 h time point *t* test, $n$=3, $p$<0.05), despite a lack of difference in viable tumor mass assessed by BLI. qRT-PCR confirmed these data demonstrating differential miR-10b expression between the miR-10b-inhibited and miR-10b-active tumors (Fig. 3c).

*Ex vivo* examination of tumor tissues confirmed the observed differential fluorescence intensity between miR-10b-inhibited and miR-10b-active tumors and confirmed that fluorescence in the miR-10b active group associated with tumor cells (Fig. 3d).

In a more clinically relevant model, we illustrated the application of the nanosensor in nude mice implanted bilaterally with the highly invasive MDA-MB-231 and the noninvasive MCF-7 breast cancer cell lines. After intravenous injection of the nanosensor, we observed significantly higher fluorescence in the MDA-MB-231 tumors than the MCF-7 tumors (Fig. 4a), corresponding to a significant difference in radiant efficiency (Fig. 4b, 63±6 % enhancement at the 15-h time point, *t* test, $n$=3, $p$<0.05). This difference was most pronounced at 15–24 h after injection of the nanosensor (Fig. 4a, b) and reflected a difference in the expression levels of miR-10b between the invasive MDA-MB-231 and noninvasive MCF-7 tumors (Fig. 4c). Finally, fluorescence microscopy confirmed the differential fluorescence between the two tumors and revealed that the activated oligo resided in the cytosol of the tumor cells (Fig. 4d).

The *in vivo* kinetics of the signal is expected. A 15- to 24-h range represents 1.5–2 blood half-lives of the nanosensor in mice. Therefore, at the time of maximum fluorescence intensity, about 25 % of the original injected dose would still exist in the circulation and would contribute to an increase in

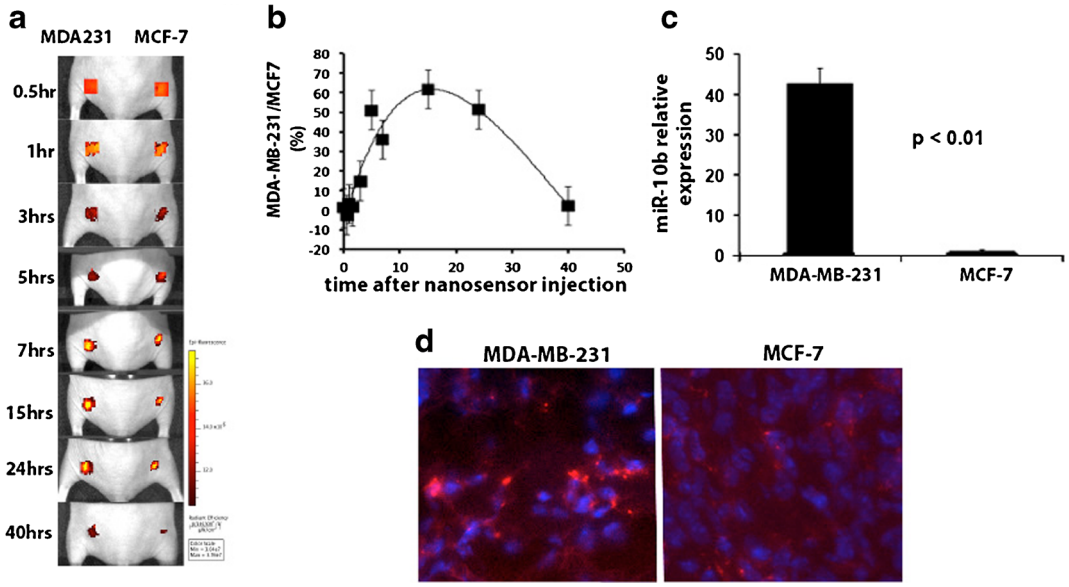


**Fig. 4** *In vivo* detection of miR-10b expression using the nanosensor in mice bilaterally implanted with MDA-MB-231 and MCF-7 cells. **a** Fluorescence optical imaging showed differential fluorescence intensity from the two tumors (i.v., 15 mg/kg Fe; 1.7 mg/kg sensor oligo). **b** Quantification of radiant efficiency showed a peak of differential radiant efficiency at 15–24 h after nanosensor injection. **c** qRT-PCR expression demonstrated significantly higher expression of miR-10b in the MDA-MB-231 tumors (data represent average±SD; two-tailed *t* test; *n*=3). **d** Fluorescence microscopy of tumor tissues from MDA-MB-231 and MCF-7 tumors. Cy5 radiant efficiency from the activated nanosensor was higher in the MDA-MB-231 tumors than in the MCF-7 tumors (blue—DAPI, nuclei; red—Cy5, activated nanosensor).

background signal. However, at later time points, the relative contribution of nanosensor in the tumor circulation vs inside tumor cells would be reduced due to nanosenser clearance. At that point, most of the fluorescence signal from tumor tissues is expected to be coming from activated sensor oligo inside tumor cells. However, because of a time lag in the passive delivery of the nanosensor into tumor tissues through the EPR effect, there would be a longer activation time *in vivo* than expected from the kinetics of the RNAi process.

After dynamic fluorescence signal quantification, the suggested mechanism of nanosensor activation is as follows. At the early time points, there is a large amount of nanosensor in the blood, but the oligo is intact (not cleaved) and therefore mostly "dark." Consequently, the changes in fluorescence at these time points would reflect nanosensor pharmacodynamics (Suppl Figs. 1a and 2a). At 15–24 h, the nanosensor is localized in tumor tissues and continuously taken up by cells, leading to the cleavage (activation) of the oligo. However, at that time point, the cleavage products have not yet been exocytosed/cleared, resulting in a dramatic and rapid increase in fluorescence (Suppl. Figs. 1b and 2b). After 24 h, the cleaved products are secreted by the tumor cells and cleared through the circulation, leading to a loss of fluorescence (Suppl. Figs. 1b and 2b). This hypothesis is consistent with our earlier findings, indicating exocytosis of the oligonucleotide fragments after cleavage [2].

## Discussion

With the goal of gaining a better understanding of the role of miRNA in cancer and of making miRNA-based diagnostics possible, we have developed technology for the profiling of tumor miRNAs *in vivo*. In these early feasibility studies, the nanoparticle-conjugated oligo was terminally labeled with the dye and the quencher. Consequently, the two were separated by 22 nucleotides (7.5 nm). However, it is possible to optimize the oligo by introducing internal labels and using alternative dye-quencher pairs. For example, if we have a 10-nucleotide (nt) distance (3.4 nm) between the dye and quencher, that would result in a distance of of 3.4 nm (10×3.4 Å/nucleotide=34 Å=3.4 nm). For the IRDye 700DX-QC-1 pair for example, the expected quenching efficiency at that distance will be 98.8 % (Li-COR Biosciences, Lincoln, NE).

In our studies, we demonstrated that the technology allows for profiling tumor miRNA signatures *in vivo*. This is important because it is only through *in vivo* studies that one can capture the true dynamics of cancer initiation and progression. Since the method is completely noninvasive, it will be possible to collect time-course data in genuine physiologic environments and thus gain a better understanding of individual-to-individual variation, authentic molecular processes, and long-term trends.

In a laboratory setting, the tools developed here can lead to the mapping out of a comprehensive and systematic atlas of cancer progression. In a clinical setting, the technology

will facilitate early cancer detection and/or cancer risk assessment and facilitate/accelerate the process of drug discovery.

With specific relevance to clinical application, the nanocarrier component of the nanosensors is based on a clinically approved nanoparticle [36, 37]. Consequently, a derivative of the developed technology may one day become applicable in a clinical setting and as such has the potential of advancing our ability to diagnose and treat breast cancer.

A variety of scenarios could benefit from the described technology. For example, it has been established that miR-10b is upregulated in the tumors of patients who harbor metastatic disease, indicating that miR-10b could be used to diagnose the presence of metastasis or even to forecast invasive disease [25, 38, 39]. The ability to detect miR-10b upregulation in the primary tumors by noninvasive or laparoscopic methods that specifically target a suspected lesion would be highly clinically beneficial.

miR-10b is also part of a panel of miRNAs that demonstrate aberrant expression in tissues from patients with triple negative breast cancer that displays chemoresistance [40]. In this context, noninvasive or laparoscopic imaging can help guide therapeutic decisions.

These are just a few examples of how the described nanosensors could be of preclinical and clinical value. However, the list of miRNAs implicated in various aspects of tumorigenesis is poised to expand rapidly over the next decade. In addition, the knowledge about the precise roles of each of the roughly 1500 known human miRNAs is increasingly becoming more focused, as specific targets are being identified and validated *in vitro*. Consequently, the development of similar technologies for miRNA-based diagnostics will inevitably represent an element of precision medicine, defined by rational drug design, individualized intervention, and targeted image-guided delivery of therapy.

## Conclusions

Considering that microRNAs represent highly specific and very early and/or predictive biomarkers of metastatic potential, risk assessment, prognosis, and treatment response, the described methodology can help acquire a better understanding of the epigenetic mechanisms underlying cancer emergence and progression. This knowledge could ultimately assist in forecasting invasive disease and predicting response to specific therapeutic modalities, leading to the design of individualized curative or even preventive treatments. In the long run, since magnetic nanoparticles are already in clinical use and the technology for optical imaging of the breast is gaining clinical relevance, one can envision a utility for our method in application to image-guided laparoscopic or intraoperative diagnostics.

*Acknowledgments.* The authors would like to acknowledge the National Institutes of Health (R01CA16346101A1 from the National Cancer Institute to ZM and 5T32CA009502 to AM) and the Breast Cancer Alliance (Young Investigator Award to ZM) for funding support.

*Funding.* The study was supported under grants R01CA16346101A1 from the National Cancer Institute to ZM, the Young Investigator Award by the Breast Cancer Alliance to ZM, and 5T32CA009502 to AM.

## References

1. Ling H, Fabbri M, Calin GA (2013) MicroRNAs and other non-coding RNAs as targets for anticancer drug development. Nat Rev Drug Discov 12:847–865
2. Yoo B, Kavishwar A, Ghosh SK et al (2014) Detection of miRNA expression in intact cells using activatable sensor oligonucleotides. Chem Biol 21:199–204
3. Bracken CP, Szubert JM, Mercer TR et al (2011) Global analysis of the mammalian RNA degradome reveals widespread miRNA-dependent and miRNA-independent endonucleolytic cleavage. Nucleic Acids Res 39:5658–5668
4. Pohlmann C, Sprinzl M (2010) Electrochemical detection of microRNAs via gap hybridization assay. Anal Chem 82:4434–4440
5. Song R, Ro S, Yan W (2010) *In situ* hybridization detection of microRNAs. Methods Mol Biol 629:287–294
6. Li W, Zhao B, Jin Y, Ruan K (2010) Development of a low-cost detection method for miRNA microarray. Acta Biochim Biophys Sin (Shanghai) 42:296–301
7. Husale S, Persson HH, Sahin O (2009) DNA nanomechanics allows direct digital detection of complementary DNA and microRNA targets. Nature 462:1075–1078
8. Mandir JB, Lockett MR, Phillips MF et al (2009) Rapid determination of RNA accessible sites by surface plasmon resonance detection of hybridization to DNA arrays. Anal Chem 81:8949–8956
9. Driskell JD, Primera-Pedrozo OM, Dluhy RA et al (2009) Quantitative surface-enhanced Raman spectroscopy based analysis of microRNA mixtures. Appl Spectrosc 63:1107–1114
10. Havelda Z (2010) *In situ* detection of miRNAs using LNA probes. Methods Mol Biol 592:127–136
11. Lu J, Tsourkas A (2009) Imaging individual microRNAs in single mammalian cells *in situ*. Nucleic Acids Res 37:e100
12. Nuovo GJ, Elton TS, Nana-Sinkam P et al (2009) A methodology for the combined *in situ* analyses of the precursor and mature forms of microRNAs and correlation with their putative targets. Nat Protoc 4:107–115
13. Silahtaroglu AN, Nolting D, Dyrskjot L et al (2007) Detection of microRNAs in frozen tissue sections by fluorescence *in situ* hybridization using locked nucleic acid probes and tyramide signal amplification. Nat Protoc 2:2520–2528
14. Nelson PT, Baldwin DA, Scearce LM et al (2004) Microarray-based, high-throughput gene expression profiling of microRNAs. Nat Methods 1:155–161
15. Moore A, Weissleder R, Bogdanov A Jr (1997) Uptake of dextran-coated monocrystalline iron oxides in tumor cells and macrophages. J Magn Reson Imaging 7:1140–1145
16. Fabian MR, Sonenberg N (2012) The mechanics of miRNA-mediated gene silencing: a look under the hood of miRISC. Nat Struct Mol Biol 19:586–593
17. van Rooij E, Kauppinen S (2014) Development of microRNA therapeutics is coming of age. EMBO Mol Med 6:851–864
18. Hartig JS, Grune I, Najafi-Shoushtari SH, Famulok M (2004) Sequence-specific detection of MicroRNAs by signal-amplifying ribozymes. J Am Chem Soc 126:722–723
19. Ko HY, Hwang W, Lee DS, Kim S (2009) A reporter gene imaging system for monitoring microRNA biogenesis. Nat Protoc 4:1663–1669
20. Cissell KA, Rahimi Y, Shrestha S et al (2008) Bioluminescence-based detection of microRNA, miR21 in breast cancer cells. Anal Chem 80:2319–2325
21. Tu Y, Li W, Wu P et al (2013) Fluorescence quenching of graphene oxide integrating with the site-specific cleavage of the endonuclease for sensitive and selective microRNA detection. Anal Chem 85:2536–2542
22. Yigit MV, Ghosh SK, Kumar M et al (2013) Context-dependent differences in miR-10b breast oncogenesis can be targeted for the prevention and arrest of lymph node metastasis. Oncogene 32:1530–1538
23. Ma L, Teruya-Feldstein J, Weinberg RA (2007) Tumour invasion and metastasis initiated by microRNA-10b in breast cancer. Nature 449:682–688

24. Ma L, Reinhardt F, Pan E et al (2010) Therapeutic silencing of miR-10b inhibits metastasis in a mouse mammary tumor model. Nat Biotechnol 28:341–347
25. Baffa R, Fassan M, Volinia S et al (2009) MicroRNA expression profiling of human metastatic cancers identifies cancer gene targets. J Pathol 219:214–221
26. Tromberg BJ, Pogue BW, Paulsen KD et al (2008) Assessing the future of diffuse optical imaging technologies for breast cancer management. Med Phys 35:2443–2451
27. Lee BT, Hutteman M, Gioux S et al (2010) The FLARE intraoperative near-infrared fluorescence imaging system: a first-in-human clinical trial in perforator flap breast reconstruction. Plast Reconstr Surg 126:1472–1481
28. Bhushan KR, Misra P, Liu F et al (2008) Detection of breast cancer microcalcifications using a dual-modality SPECT/NIR fluorescent probe. J Am Chem Soc 130:17648–17649
29. Yoo B, Ghosh SK, Kumar M et al (2014) Design of nanodrugs for miRNA targeting in tumor cells. J Biomed Nanotechnol 10:1114–1122
30. Medarova Z, Pham W, Farrar C et al (2007) *In vivo* imaging of siRNA delivery and silencing in tumors. Nat Med 13:372–377
31. Kumar M, Yigit M, Dai G et al (2010) Image-guided breast tumor therapy using a small interfering RNA nanodrug. Cancer Res 70:7553–7561
32. Wang J, Sui M, Fan W (2010) Nanoparticles for tumor targeted therapies and their pharmacokinetics. Curr Drug Metab 11:129–141
33. Akinc A, Thomas M, Klibanov AM, Langer R (2005) Exploring polyethylenimine-mediated DNA transfection and the proton sponge hypothesis. J Gene Med 7:657–663
34. Hong S, Leroueil PR, Majoros IJ et al (2007) The binding avidity of a nanoparticle-based multivalent targeted drug delivery platform. Chem Biol 14:107–115
35. Weissleder R, Kelly K, Sun EY et al (2005) Cell-specific targeting of nanoparticles by multivalent attachment of small molecules. Nat Biotechnol 23:1418–1423
36. Harisinghani MG, Barentsz J, Hahn PF et al (2003) Noninvasive detection of clinically occult lymph-node metastases in prostate cancer. N Engl J Med 348:2491–2499
37. Michel SC, Keller TM, Frohlich JM et al (2002) Preoperative breast cancer staging: MR imaging of the axilla with ultrasmall superparamagnetic iron oxide enhancement. Radiology 225:527–536
38. Chen W, Cai F, Zhang B et al (2013) The level of circulating miRNA-10b and miRNA-373 in detecting lymph node metastasis of breast cancer: potential biomarkers. Tumour Biol 34:455–462
39. Iyevleva AG, Kuligina E et al (2012) High level of miR-21, miR-10b, and miR-31 expression in bilateral vs. unilateral breast carcinomas. Breast Cancer Res Treat 131:1049–1059
40. Ouyang M, Li Y, Ye S et al (2014) MicroRNA profiling implies new markers of chemoresistance of triple-negative breast cancer. PLoS ONE 9:e96228